

Modulating thermo-diffusion/galvanic coupling via ion speciation engineering enables high-performance ionic thermoelectric cells

Received: 29 August 2025

Accepted: 14 January 2026

Published online: 31 January 2026

Check for updates

Yuchen Li^{1,6}, Ying-Ru Qiu^{2,6}, Jinsha Liao³, Helios Y. Li¹, Zhouyuntong Liu¹, Yuxiang Chen¹, Mao Yu⁴, Lizhi Xu¹, Chang Liu⁵, Jefferson Zhe Liu³, Jian-Feng Li², Weishu Liu⁴, Yao-Hui Wang²✉ & Nicholas X. Fang¹✉

Ionic thermoelectric (i-TE) materials have demonstrated a high thermopower in harvesting low-grade heat, emerging as superior candidates for self-powered electronics. However, coupling two i-TE effects in n-type materials is scarce, which restricts the development of high-performance systems. Herein, we uncover an overlooked thermogalvanic redox reaction between Cu^{2+} and Cu^+ stabilized by Cl^- and quantitatively track the progressive reaction process by operando characterization. In binary polyvinyl alcohol (PVA)- CuCl_2 gels, an interactive i-TE coupling effect driven by ion speciation is validated, which exhibits an enhanced thermogalvanic redox as CuCl_2 concentrations increase while suppressing the thermodiffusion contribution. By distinguishing and quantifying coordination species, we reveal the impact of $[\text{Cu-Cl}]$ speciation on the i-TE effect contributions. Correspondingly, a giant thermopower of -30.6 mV K^{-1} and a remarkable power density of $0.6 \text{ mW m}^{-2} \text{ K}^{-2}$ are achieved, respectively, by tuning ion coordination speciation. The long-term power generation exhibits a reversible and sustainable heat-to-electricity conversion. High output voltage of 3.5 V and power of 22 μW are produced in 16-cell i-TE modules when harvesting 15 K. Our findings reveal an interactive thermo-diffusion/galvanic coupling effect based on coordination chemistry, offering a potential design principle for high-performance i-TE materials.

Low-grade waste heat, the ubiquitous byproduct of natural or industrial processes, can be generated from solar energy, geothermal energy, manufacturing, and even the human body, representing a massive and untapped resource^{1–3}. Most of this heat exists below

100 °C, making it difficult for conventional power generation. Existing technology, such as electronic-thermoelectric generators (e-TEGs), can convert such heat into electricity; however, their high costs (e.g., rare metal elements) and low thermopower (or Seebeck coefficient)

¹Department of Mechanical Engineering, The University of Hong Kong, Hong Kong, China. ²College of Materials, State Key Laboratory of Physical Chemistry of Solid Surfaces, College of Chemistry and Chemical Engineering, College of Energy, Xiamen University, Xiamen, China. ³Department of Mechanical Engineering, The University of Melbourne, Parkville, VIC, Australia. ⁴Department of Materials Science and Engineering & Institute of Innovative Materials, Guangdong Provincial Key Laboratory of Functional Oxide Materials and Devices, Southern University of Science and Technology, Shenzhen, China.

⁵Department of Mechanical Engineering, National University of Singapore, Singapore, Singapore. ⁶These authors contributed equally: Yuchen Li, Ying-Ru Qiu.

✉ e-mail: yaohuiwang@xmu.edu.cn; nicxfang@hku.hk

(e.g., $\sim 100\text{--}200\ \mu\text{V K}^{-1}$) limit their broad applications^{4–6}. Ionic thermoelectric (i-TE) gels represent an emerging class of soft and flexible materials that generate electricity from low-grade heat sources using ions instead of electrons^{7,8}. These gels are inexpensive to produce, and recent advances have shown they can achieve an exceptionally high thermopower of dozens of mV K^{-1} (refs. 9,10). However, a bottleneck remains. Some i-TE gels produce high voltages by thermodiffusion of charge carriers, but the output lasts only in short bursts¹¹, while others provide steady power through temperature-dependent redox reaction (thermogalvanic effects), but with disappointingly low voltages^{12,13}. Recent efforts exemplified in the pioneering work by Liu et al., i.e., gelatin-KCl-Fe(CN)₆^{4/3-} p-type gels, which demonstrate the potential of hybrid i-TE mechanisms¹⁴. Their ternary system synergized thermodiffusion and thermogalvanic effects, significantly improving both thermopower and output power.

On the other hand, n-type analogs, essential for constructing practical thermoelectric devices, also undergo similar limitations. There remain underexplored synergy mechanisms or material systems, despite the rapid development over the past years. Thermodiffusion-based gels always employed metal salts or ionic liquids, showing a remarkable negative thermopower, such as polyethylene (PEO)-LiTFSI-EmimBF₄ with $-15\ \text{mV K}^{-1}$ (ref. 15.), polyvinyl alcohol (PVA)/cellulose-CuCl₂ with $-26.3\ \text{mV K}^{-1}$ (ref. 16), and bacterial cellulose-CaCl₂ with $-27.2\ \text{mV K}^{-1}$ (ref. 17). Gels with typical n-type redox couples, including Fe^{3+/2+} (ref. 18), [Co(bpy)₃]^{3+/2+} (ref. 19), and I/I₃⁻ (refs. 20,21) are widely investigated, showing a sustainable output performance. The above research optimized i-TE properties either in thermopower or output power, but still cannot realize them simultaneously. A key unexplored opportunity lies in coupling thermodiffusion and thermogalvanic effects in n-type systems. As a model system, we uncover a hidden thermogalvanic mechanism in CuCl₂-based gels, in which Cl⁻ ions regulate the interaction of interfacial redox reactions and bulk thermodiffusion, enabling the achievement of continuous output current from electrodes to an external circuit and high built-in thermal voltage, respectively. Inspired by the early studies on copper-based redox flow batteries^{22,23}, Cu⁺ ions can be stabilized through coordination chemistry via halogen (e.g., Cl⁻). Temperature gradient induces reversible $\text{Cu}^{2+} + e \leftrightarrow \text{Cu}^+$ redox reaction, stabilized by Cl⁻ ligands to form $[\text{Cu-Cl}_y(\text{H}_2\text{O})_{6-y}]^{2-y}/[\text{Cu-Cl}_2]^-$ ($y = 0\text{--}2$, which represents the coordination number of Cl⁻) redox couples. Crucially, Cl⁻ plays dual roles: one is as the thermodiffusion carriers under the Soret effect, generating negative thermopower; the other is as coordination ligands for Cu²⁺/Cu⁺ redox couples, producing a positive temperature coefficient (equivalent to negative thermopower). These two i-TE processes exhibit an interactive coupling due to the competition of Cl⁻, and their relative contributions can be regulated by adjusting the concentration of CuCl₂. This is relatively different from the reported p-type gelatin-KCl-Fe(CN)₆^{4/3-} synergistic i-TE system, in which the KCl and Fe(CN)₆^{4/3-} were employed as thermodiffusion ion providers and thermogalvanic redox couple, respectively, showing a “synergistic-coupling” effect in parallel. Particularly, increasing CuCl₂ concentration promotes the output performance (more thermogalvanic redox species) while suppressing the thermal voltage. Modulating the thermo-diffusion/galvanic coupling via speciation engineering offers a rational strategy to achieve both high voltage and continuous power output within a single system, addressing the long-standing trade-off between the intermittent behavior of i-TE capacitors and the low voltage of i-TE generators.

Unlike prior hybrid designs that require complex multi-component gels^{24,25}, our work reports a simple binary system guided by coordination chemistry, specifically PVA-CuCl₂, which can surpass state-of-the-art n-type materials. For the first time, operando surface-enhanced Raman scattering (SERS) was employed to quantify the coordination evolution, in combination with density functional theory (DFT) calculations, to reveal thermogalvanic redox pathways. In

addition, the coordination [Cu-Cl] complexes were identified using UV-vis spectroscopy combined with molecular dynamics (MD) simulations to determine their quantitative distribution, revealing a correlation with the i-TE performance. By modulating ion speciation, we achieved a giant thermopower of $-30.6\ \text{mV K}^{-1}$ and a remarkable output power performance of $0.60\ \text{mW m}^{-2}\ \text{K}^{-2}$ in the PVA-CuCl₂ i-TE system. In 16-cell modules, ultrahigh output voltage of 3.5 V and output power of 22 μW were generated when harvesting a low-grade heat of 15 K. This approach not only circumvents the limitations of the solid-state thermoelectric but also provides a promising strategy to achieve both high thermal voltage and power output in flexible i-TE systems.

Uncovering the overlooked thermogalvanic effect

Copper-based systems have been widely investigated in both i-TE solutions and gels. Copper electrodes were consumed unsustainably in CuSO₄ solutions to construct the Cu²⁺/Cu⁰ redox couple²⁶. The CuCl₂ has been widely employed as a common active salt for thermodiffusion in the previous i-TE gels^{16,27–30}. However, the impact of the thermogalvanic effect, associated with the redox reaction of Cu²⁺/Cu⁺ stabilized by the Cl⁻, has been overshadowed in the literature so far. Electrochemical characterization of PVA-*x* CuCl₂ (*x* from 0.05 to 1.7 M) i-TE cells firstly revealed a pronounced enhancement in thermogalvanic redox reaction activity. The detailed fabrication process of as-prepared i-TE gels and cells was demonstrated in Supplementary Fig. 1. The morphology and mechanical properties of the PVA-1.0 M CuCl₂ i-TE gels are shown in Supplementary Figs 2 and 3, exhibiting a 3D interconnected and porous structure and high break elongation of $\sim 250\%$. Cyclic voltammetry (CV) showed a near two-order-of-magnitude increase in faradaic current density (j_D in Fig. 1a), while redox reaction peak potentials (E_D) shifted cathodically with increasing *x* (Supplementary Fig. 4). Electrochemical impedance spectroscopy (EIS) further corroborated accelerated kinetics, showing a four-order-of-magnitude reduction in charge transfer resistance (R_{ct}) (Fig. 1b and c, and Supplementary Fig. 5). These trends align with the growing population of redox reaction couples, which facilitate faster electron transfer. The interplay between thermodiffusion and thermogalvanic contributions was quantified through thermal voltage (V_{oc}), short-circuit current density (I_{sc}), and instantaneous maximum power density (P_{max}) (Fig. 1d and Supplementary Fig. 6). An opposite trend of i-TE performance was demonstrated: decreasing V_{oc} and increasing I_{sc} with increasing *x*. This concentration-dependent trade-off underscores the crucial role of speciation in optimizing i-TE performance, specifically the highest thermal voltage at $x = 0.1\ \text{M}$ and the highest output power at $x = 1.5\ \text{M}$. According to the linear V - I curves, we calculated the internal resistance of PVA-*x* CuCl₂ i-TE cells and discussed feasible strategies of further improving output power performance (Supplementary Fig. 7 and Supplementary Note 1). As a result, normalized output power ($P_{max}/(\Delta T)^2$) values ranging from 0.09 to $0.43\ \text{mW m}^{-2}\ \text{K}^{-2}$ were achieved in binary PVA-*x* CuCl₂ gels, as *x* increased from 0.1 to 1.5 M, showing a great advantage compared with other intrinsic n-type thermogalvanic redox couples, including Fe^{2+/3+}, [Co(bpy)₃]^{2+/3+}, and I/I₃⁻ (Fig. 1e and Supplementary Table 1). Furthermore, the thermopower of PVA-0.1 M CuCl₂ showed a giant value among the reported i-TE gels based on thermodiffusion or thermogalvanic effect (Fig. 1f and Supplementary Table 2). Binary PVA-CuCl₂ gels exhibit both promising advantages in thermopower and output performance due to the coupling effect of thermodiffusion and thermogalvanic.

Thermo-diffusion/galvanic coupling mechanism

To investigate the speciation-dependent coupling of thermodiffusion and thermogalvanic effects, we systematically varied the CuCl₂ concentrations (*x*) from 0.01 to 2 M in the PVA-*x* CuCl₂ gels. Density functional theory (DFT) calculations revealed the free energies of possible coordination species and predicted the three prominent redox couples (Fig. 2a, Supplementary Figs. 8 and 9, as detailed in

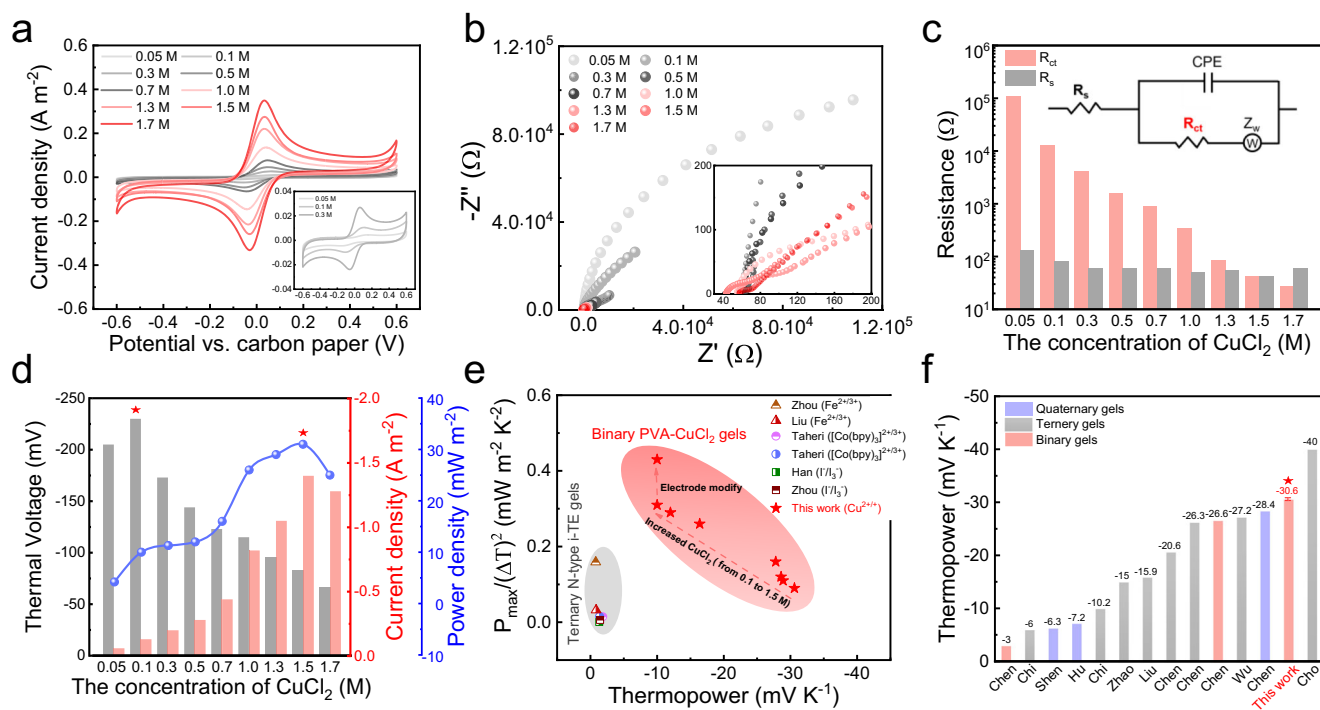


Fig. 1 | Uncovering the overlooked thermogalvanic effect. The CuCl_2 concentrations (x) range from 0.05 to 1.7 M. **a** Cyclic voltammetry (CV) curves. The inset picture is the enlarged view for the $x = 0.05, 0.1$, and 0.3 M. **b** Electrochemical Impedance Spectroscopy (EIS) curves. The inset picture is the enlarged view at high-frequency ranges. **c** Fitted values of the charge transfer resistance (R_{ct}) and internal resistance (R_s) of PVA- x CuCl_2 i-TE cells. The inset picture is the corresponding equivalent circuit. **d** Combination curves of saturated thermal voltage,

short-circuit current density, and instantaneous maximum output power density. The applied temperature difference is 10 K. **e** Comparison of the normalized output power density and thermopower of the binary PVA- x CuCl_2 i-TE cells with other reported ternary n-type thermogalvanic i-TE cells. **f** Comparison of the thermopower of PVA-0.1 M CuCl_2 gel with other reported n-type state-of-the-art multi-component i-TE gels.

Supplementary Note 2). Three dominant oxidized species with the lowest negative free energy were demonstrated: fully hydrated $[\text{Cu}(\text{H}_2\text{O})_6]^{2+}$ and chlorinated complexes $[\text{Cu}-\text{Cl}(\text{H}_2\text{O})_5]^+$ and $[\text{Cu}-\text{Cl}_2(\text{H}_2\text{O})_4]$ (collectively denoted as $[\text{Cu}-\text{Cl}_y(\text{H}_2\text{O})_{6-y}]^{2-y}$, $y = 0-2$). We calculated three possible reduced species (e.g., $[\text{Cu}-\text{Cl}]$, $[\text{Cu}-\text{Cl}-\text{H}_2\text{O}]$, and $[\text{Cu}-\text{Cl}_2]^-$) and finally identified $[\text{Cu}-\text{Cl}_2]^-$ as the most likely formed due to its lowest energy of 4.6 eV³¹. The operando SERS also helps to verify the reduced species, as discussed below.

Figure 2b shows the detailed ion diffusion process and redox reaction under the temperature gradient (ΔT) in PVA- x CuCl_2 systems. When giving a ΔT , the oxidized species of $[\text{Cu}-\text{Cl}_y(\text{H}_2\text{O})_{6-y}]^{2-y}$ could be reduced to $[\text{Cu}-\text{Cl}_2]^-$ at the hot electrode, then the ΔT drives the diffusion of the $[\text{Cu}-\text{Cl}_2]^-$ and promotes the oxidation at the cold electrode, thereby forming the reversible redox couple. $[\text{Cu}-\text{Cl}_2]^-$ showed a higher solvation entropy than $[\text{Cu}-\text{Cl}_y(\text{H}_2\text{O})_{6-y}]^{2-y}$, because of more freedom in the arrangement of water molecule shells due to its simple coordination configuration. For the redox reaction of $[\text{Cu}-\text{Cl}_y(\text{H}_2\text{O})_{6-y}]^{2-y} + (2-y) \text{Cl}^- + e^- \leftrightarrow [\text{Cu}-\text{Cl}_2]^- + (6-y) \text{H}_2\text{O}$, the temperature coefficient (α_R) could be defined as $\alpha_R = \frac{S_{[\text{Cu}-\text{Cl}_2]^-} - S_{[\text{Cu}-\text{Cl}_y(\text{H}_2\text{O})_{6-y}]^{2-y}}}{F} > 0$, where F is the Faraday constant. On the other hand, the chelation interactions between Cu^{2+} with the hydroxyls of PVA restricted its translational migration freedom^{16,28,32}, leading to a higher thermal mobility of Cl^- ($D\hat{S}/k_B T$, D : diffusion coefficient and \hat{S} : Eastman entropy)¹⁴, which determines a negative thermodiffusive thermopower. Generally, a positive temperature coefficient (negative thermopower attributed to thermogalvanic effect) and a negative thermodiffusive thermopower could be synergistically combined (as detailed in Supplementary Note 3).

Unlike the single synergistic effect^{14,33,34}, the thermo-diffusion/galvanic coupling in PVA- x CuCl_2 gels exhibits a trade-off relationship

due to the competition of Cl^- . This mechanism leads to an opposite trend of i-TE performance as x increases: achieving high output power driven by $[\text{Cu}-\text{Cl}_y(\text{H}_2\text{O})_{6-y}]^{2-y}/[\text{Cu}-\text{Cl}_2]^-$ redox couples while decreasing the thermal voltage mainly from the thermodiffusion contribution, which could be attributed to coordinated species evolution. We found that the proportion of $[\text{Cu}(\text{H}_2\text{O})_6]^{2+}$ decreased from 96.7% to 36.4%, while the $[\text{Cu}-\text{Cl}]$ species (a joint name of species with Cl^- coordination) increased from 2.8% to 49.9% (from MD results), as the x increased from 0.01 to 2 M. Compared with the $[\text{Cu}(\text{H}_2\text{O})_6]^{2+}$, $[\text{Cu}-\text{Cl}]$ species showed a weaker hydration structure, suggesting a faster diffusion rate^{16,35}. The suppression of the thermodiffusion effect from two sides: one is the increased cation diffusion coefficient (D_+) driven by $[\text{Cu}-\text{Cl}]$ clusters; the other is that the competition of Cl^- in the thermogalvanic redox reaction leads to a decrease of thermal mobility of $D\hat{S}/k_B T$. The interaction relationship between two i-TE effects could be modulated just by manipulating the ion concentrations, endowing dual i-TE performance in a single system, i.e., high thermopower (at low x of 0.1 M) and output performance (at high x of 1.5 M).

Revealing the thermogalvanic redox process by operando SHINERS

Raman spectroscopy has been used to observe the ion thermodiffusion process at electrode surfaces³⁶ or to reveal the redox reaction in aqueous thermogalvanic cells². However, Raman investigations in hydrogel systems are primarily challenged by the weak signals, which also lack quantitative analysis. Here, we employed an advanced SERS technique called shell-isolated nanoparticle-enhanced Raman spectroscopy (SHINERS)³⁷, quantitatively revealing the coordination evolution within the thermogalvanic redox reaction. The synthesis of shell-isolated nanoparticles (SHINs), Au@SiO₂ core-shell nanoparticles, is reported in refs. 37,38. The inert silica shell prevented direct

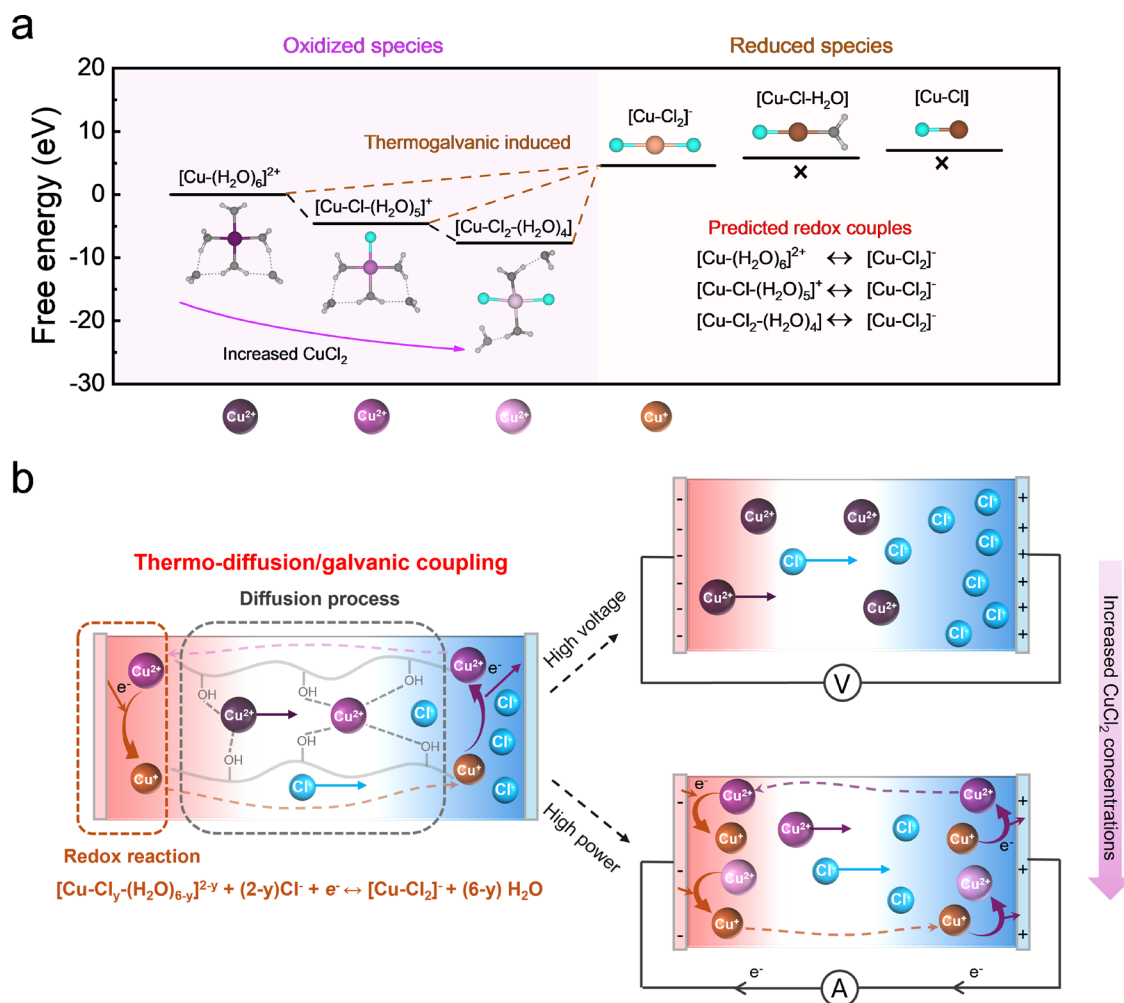


Fig. 2 | Thermo-diffusion/galvanic coupling mechanism. **a** Free energy of the main oxidized and reduced species and predicted redox reaction pathways. **b** Schematic figure of the thermo-diffusion/galvanic coupling mechanism, including ion diffusion process and redox reaction under the temperature gradient.

interaction between the plasmonic Au cores (Raman signal amplifier) and the samples to be probed, ensuring unperturbed vibrational data. This setup enabled sensitive, non-destructive detection across diverse substrates, leveraging strong enhanced electromagnetic fields at nanoparticle-substrate junctions to amplify signals by millions of times.

In our experiments, SHINs were uniformly deposited onto the surface of i-TE gels (Supplementary Fig. 10). The operando SHINERS test was conducted in a PVA-0.1M CuCl_2 gel under a ΔT of 10 K, collecting signals from the top surface of the gel (near cold electrodes T_C) (Fig. 3a). As thermal charging time (t) increased from 0 to 30 mins, the Raman peak of $[\text{Cu}-\text{Cl}_2]^-$ approximately at 261 cm^{-1} significantly increased, attributed to migration of reduction product from the T_H to T_C (Fig. 3b). While the Raman peak of $[\text{Cu}-(\text{H}_2\text{O})_6]^{2+}$ approximately at 420 cm^{-1} (refs. 16,30.) gradually decreases, indicating the coordination environment change from $[\text{Cu}-\text{H}_2\text{O}]$ to $[\text{Cu}-\text{Cl}]$. We also conducted an isotopic substitution (D_2O) experiment to verify the $[\text{Cu}-\text{H}_2\text{O}]$ Raman peak (Supplementary Fig. 11). Then, without ΔT , the redox reaction stopped, and the species gradually distributed in equilibrium, decreasing the intensity of $[\text{Cu}-\text{Cl}_2]^-$. The test was also conducted in the cross-section of the gel to further observe the migration of redox species inside the gel (Supplementary Fig. 12). To correlate coordination species changes with valence states, we complemented SHINERS with XPS mapping of Cu^{2+} and Cu^+ distribution near the surface of the gel. The Cu^{2+} ($\text{Cu } 2p_{3/2}$ and $\text{Cu } 2p_{1/2}$ peaks at 935.1 and 955 eV,

respectively) and Cu^+ ($\text{Cu } 2p_{3/2}$ and $\text{Cu } 2p_{1/2}$ peaks at 932.3 and 952 eV, respectively) were detected at both sides after thermal charging, showing a larger intensity of Cu^{2+} than Cu^+ at the gel bottom while reversing at the gel top^{27,28,30} (Fig. 3c). Not only in the gel surface, but we also combined the X-ray absorption near-edge structure (XANES) characterization to further confirm the existence of $\text{Cu}^{2+}/\text{Cu}^+$ redox couple ions in the i-TE gel bulk (Supplementary Fig. 13). Furthermore, we proposed a methodology to quantify a normalized $[\text{Cu}-\text{Cl}]$ factor defined by integrating the $[\text{Cu}-\text{Cl}]$ Raman peak area. The $[\text{Cu}-\text{Cl}]$ factors increased from 1 to 3.58 as t increased from 0 to 30 mins and then decreased to 1.80 without ΔT , corresponding to the thermal voltage decreased from -2 to -234 mV, and then recovered to -9 mV (Fig. 3d). The higher $[\text{Cu}-\text{Cl}]$ factors were observed at higher x , suggesting promoted thermogalvanic redox reactions (Supplementary Fig. 14, Tables 3 and 4). Our experimental characterization, combining SHINERS with surface analytical XPS characterization, is readily adaptable to other redox reaction-active hydrogels or soft-material systems, enabling precise mapping of both coordination and electronic states under operando conditions.

We further verified the redox reaction by electrochemical characterization. One PVA-0.1M CuCl_2 i-TE cell was operated with four thermal charging-activation cycles (Supplementary Fig. 15). After the first cycle, the j_p and R_{ct} showed a significant increase and decrease, respectively, indicating that the induced redox species facilitated the kinetics (Supplementary Fig. 16). We also compared the redox

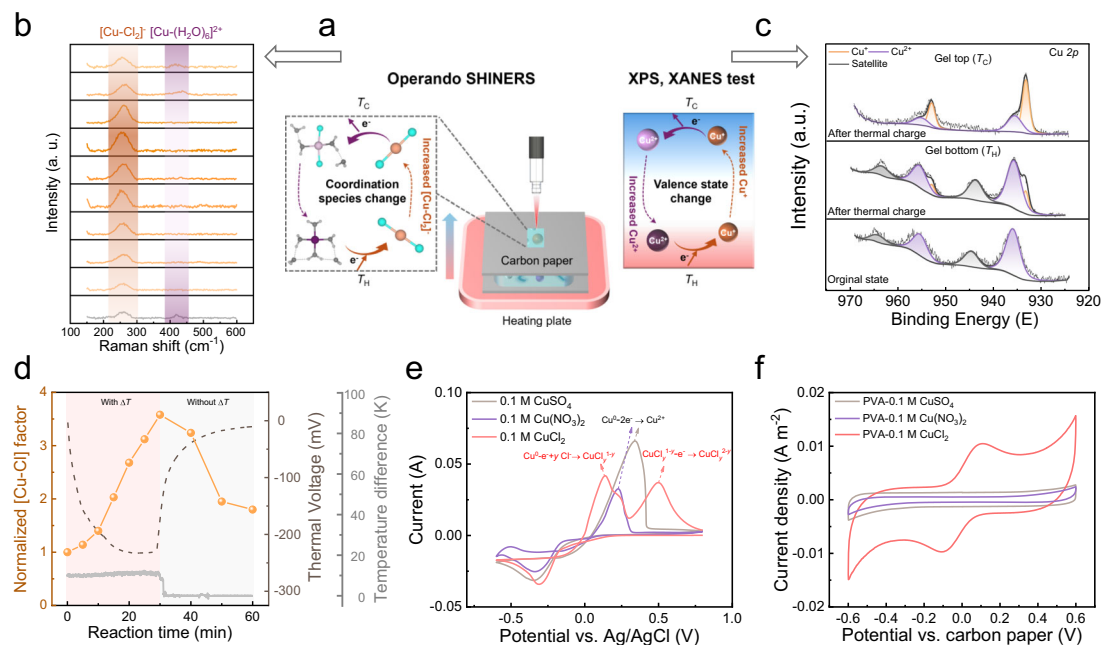


Fig. 3 | Revealing the thermogalvanic redox process by operando SHINERS.

a Diagram of the operando SHINERS, XPS, and XANES characterizations. The Raman signals were collected from the top of the gel. The XPS test was applied to the rapidly frozen-drying i-TE gel after thermal charging for 30 mins. The ΔT is constructed in the direction from the bottom to the top. **b** Raman spectra of the gel

at different reaction times during the thermal charging-reactivation process. **c** XPS results of each side of the gel at different reaction states. **d** Combination curves of the normalized Cu-Cl factors, the thermal voltage, and applied ΔT . **e** CV curves of 0.1 M CuSO_4 , 0.1 M $\text{Cu}(\text{NO}_3)_2$, and 0.1 M CuCl_2 solutions. **f** CV curves of PVA-0.1 M CuSO_4 , PVA-0.1 M $\text{Cu}(\text{NO}_3)_2$, and PVA-0.1 M CuCl_2 i-TE gels.

behaviors of i-TE systems with CuSO_4 and $\text{Cu}(\text{NO}_3)_2$, in which only $[\text{Cu}(\text{H}_2\text{O})_6]^{2+}$ species existed from UV-vis spectra (Supplementary Fig. 17). In the three-electrode CV test, two obvious anodic peaks were discovered in CuCl_2 solution due to the intermediate of Cu^+ , while only one anodic peak corresponding to Cu^0 to Cu^{2+} was observed in $\text{CuSO}_4/\text{Cu}(\text{NO}_3)_2$ solutions (Fig. 3e). Correspondingly, a pair of redox reaction peaks were observed only in the PVA-0.1 M CuCl_2 i-TE cell (Fig. 3f). The additional CaCl_2 doping could further increased redox species from CV results (Supplementary Fig. 18). The UV-vis spectra of PVA-0.1/2 M $\text{CuCl}_2/\text{CaCl}_2$ gels showed a broad absorption range from 250 to 350 nm, indicating the multiple $[\text{Cu-Cl}]$ species (Supplementary Fig. 19). The increased I_{sc} and P_{max} by doping CaCl_2 revealed the enhanced thermogalvanic effect, also indicating an effective output performance optimization strategy (Supplementary Fig. 20).

Impact of $[\text{Cu-Cl}]$ speciation on thermopower

Understanding the chemical speciation of cupric ions in chloride solutions is critical for optimizing thermoelectric energy conversion, in addition to its relevance in geochemical³⁹ and environmental⁴⁰. However, identifications of multiple chemical speciation in the CuCl_2 system have yet to emerge, especially at high concentrations⁴¹. Here, we combine molecular dynamics (MD) simulations (as detailed in Supplementary Note 4) with UV-vis spectroscopy (Integrating Sphere device) to resolve $[\text{Cu-Cl}]$ speciation across a concentration range ($x = 0.01$ to 2 M). A representative snapshot of the equilibrated molecular configuration at $x = 2.0$ M is shown in Fig. 4a, where multiple coordination species are observed (as listed in the right-side legend). Figure 4b quantitatively maps the distribution of these $[\text{Cu-Cl}]$ coordination complexes, revealing a concentration-dependent shift from fully hydration-dominated to chloride-dominated species, including polynuclear clusters. The UV-vis spectra showed a series of absorption peaks due to the ligand-to-metal charge transfer (LMCT) effect⁴¹, suggesting the complexity of the species. As the x increased from 0.01 to 2 M, the absorption peaks progressively redshifted from 220 to 400 nm (Fig. 4c), reflecting the growing contribution of higher-order

$[\text{Cu}_x\text{-Cl}_y]^{2-x}$ clusters^{42,43}, which is attributed to entropy-driven solvation restructuring. This is the key factor when correlating the decreased thermopower trend with the increased x , which will be discussed below. We conducted principal component analysis (PCA) on UV-vis spectra to estimate the number of primary species in the gels^{44,45}, showing an increased number from 2 to 5 as x increased from 0.05 to 2 M (Fig. 4d and Supplementary Fig. 21, as detailed in Supplementary Note 5). Correspondingly, the proportion of $[\text{Cu-Cl}]$ species increased from 11.9% to 49.9% (Supplementary Fig. 22). These quantitative resolutions of $[\text{Cu-Cl}]$ speciation provide a foundation for tailoring coordination species in thermoelectric systems.

Next, we correlated the output voltage performance with x . The thermal voltages showed a significant decrease with the increased x (Fig. 4e and Supplementary Figs. 23, 24, and 25). We attributed such trend to an interactive balance between two i-TE processes: thermodiffusion of $[\text{Cu-H}_2\text{O}]^{2+}$ and Cl^- (at low x), in which the high migration entropy difference generates a large ΔV_{td} ; and thermogalvanic reaction (at high x) driven by redox couple, leading to a smaller ΔE^0 (Supplementary Fig. 26) (ref. 14.). This interactive balance explains the non-monotonic trend in thermopower S_i (Fig. 4f): At low concentration ($0.01 \text{ M} \leq x \leq 0.07 \text{ M}$), the thermopower increased from -19.5 to -28.7 mV K^{-1} ; at intermediate concentration (0.1 to 0.7 M), the thermopower achieved a maximum value of -30.6 mV K^{-1} at $x = 0.1 \text{ M}$ and then gradually decreased; and at high concentration ($x \geq 1 \text{ M}$), enhanced thermogalvanic effects collapse the thermopower to -5.9 mV K^{-1} ($x = 2.0 \text{ M}$). We also use an isothermal three-electrode system to determine the temperature coefficient (α_R) of PVA- x CuCl_2 gels (Supplementary Fig. 27). The values were finally determined as 0.58, 0.64, 1.32, 1.54, 1.12, 1.05, and 0.98 mV K^{-1} as $x = 0.01, 0.05, 0.1, 0.5, 1.0, 1.5,$ and 2.0 M (Supplementary Figs. 28 and 29). The calculated thermopower contribution of two i-TE mechanisms exhibited an opposite trend, which is consistent with the coupling relationship (Supplementary Fig. 30). Combining the thermopower performance with MD results, we found that the dominant existing of $[\text{Cu}(\text{H}_2\text{O})_6]^{2+}$, $[\text{Cu-Cl}(\text{H}_2\text{O})_5]^+$, and $[\text{Cu-Cl}_2(\text{H}_2\text{O})_4]$ ($0.1 \leq x \leq 0.7 \text{ M}$) showed benefits

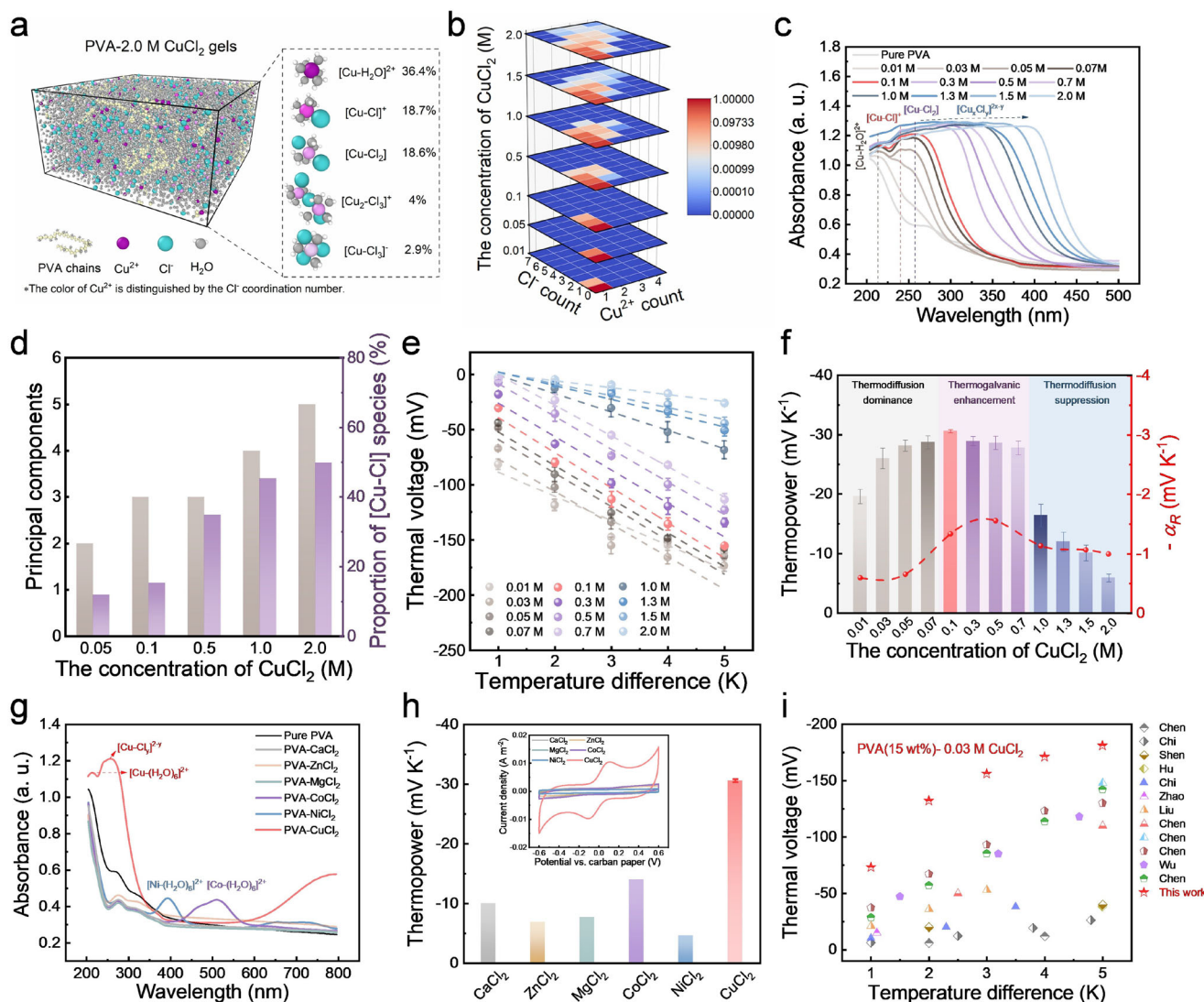


Fig. 4 | Impact of [Cu-Cl] speciation on thermopower. The CuCl_2 concentrations (x) range from 0.01 to 2 M. **a** Molecular dynamics (MD) simulations of PVA-2.0 M CuCl_2 gel. The top five species are listed in terms of proportion. **b** Heat map of the [Cu-Cl] species distribution in PVA- x CuCl_2 gels. **c** UV-vis spectra of PVA- x CuCl_2 gels. **d** Principal component analysis based on UV-vis spectra and proportions of [Cu-Cl] species from MD results at $x = 0.05, 0.1, 0.5, 1.0,$ and 2.0 M. **e** Thermal voltages of PVA- x CuCl_2 i-TE cells within ΔT of 0–5 K. **f** Total thermopower and

thermoelectric thermopower ($-\alpha_R$) of the PVA- x CuCl_2 i-TE cells. **g** UV-vis spectra of PVA-based gels with different divalent metal chlorides (the concentrations are controlled as 0.1 M). **h** Thermopower values of different divalent metal chlorides i-TE cells. The inset picture is the CV curves of the corresponding i-TE cells. **i** Comparison of the thermal voltage of the PVA (15 wt%)-0.03 M CuCl_2 i-TE cell with the values reported in other n-type i-TE gels. The corresponding ΔT range is from 1 to 5 K.

on regulating both thermodiffusive and thermogalvanic thermopower ($-\alpha$), while the formation of higher-order $[\text{Cu}_x\text{Cl}_y]^{2x-y}$ (e.g., $[\text{Cu}_2\text{Cl}_2(\text{H}_2\text{O})_8]^{2+}$ and $[\text{Cu}_2\text{Cl}_3(\text{H}_2\text{O})_8]^{+}$ etc., at $x \geq 1$ M) declined thermopower of both parts. Critically, we identify an optimal species distribution for maximizing thermopower: approximately 84.6% $[\text{Cu}(\text{H}_2\text{O})_6]^{2+}$, 12.6% $[\text{Cu}(\text{H}_2\text{O})_5]^{+}$, and 2.8% $[\text{Cu}(\text{H}_2\text{O})_4]^{2+}$, achieved in PVA-0.1 M CuCl_2 gels (Supplementary Fig. 22).

Except for [Cu-Cl] coordination species, other divalent metal chloride gels only showed water coordination environments (Fig. 4g). Compared with other divalent metal chlorides, only PVA-0.1 M CuCl_2 exhibited the thermogalvanic property and achieved the highest thermopower of -30.6 mV K^{-2} (Fig. 4h and Supplementary Fig. 31), showing a unique advantage of [Cu-Cl] coordination species on regulating thermopower. We also found that the increased weight ratio of PVA to water (r_w) can further enhance thermal voltages, probably by enhancing the chelation of PVA and Cu^{2+} (Supplementary Fig. 32). As a result, the thermal voltages of $-73, -132, -156, -171,$ and -181 mV

were optimized in PVA (15 wt%)-0.03 M CuCl_2 gel, also showing giant values within ΔT of 0–5 K (Fig. 4i, Supplementary Fig. 33 and Table 5).

Optimization of output performance and long-term power generation

A chloride-rich environment has a direct impact on boosting the output power performance in our i-TE cells by stabilizing more $\text{Cu}^{2+}/\text{Cu}^{+}$ redox couples in the thermogalvanic process. In this part, we further increased the amount of the redox couple by enriching the content of Cl^- . Different metal chlorides with the same Cl^- content (0.5 M) were doped into the PVA-0.5 M CuCl_2 i-TE cells, showing enhanced redox reaction kinetics but leading to declines in V_{oc} (Supplementary Fig. 34A to C). As a result, the optimized P_{max} was achieved by introducing the 0.25 M CaCl_2 (Fig. 5a and Supplementary Fig. 34D). Then, the concentrations of CuCl_2 were optimized, and the highest P_{max} value of 37 mW m^{-2} was obtained in the PVA-1.5/0.25 M $\text{CuCl}_2/\text{CaCl}_2$ (Supplementary Fig. 35). Finally, the concentrations of CaCl_2 were further

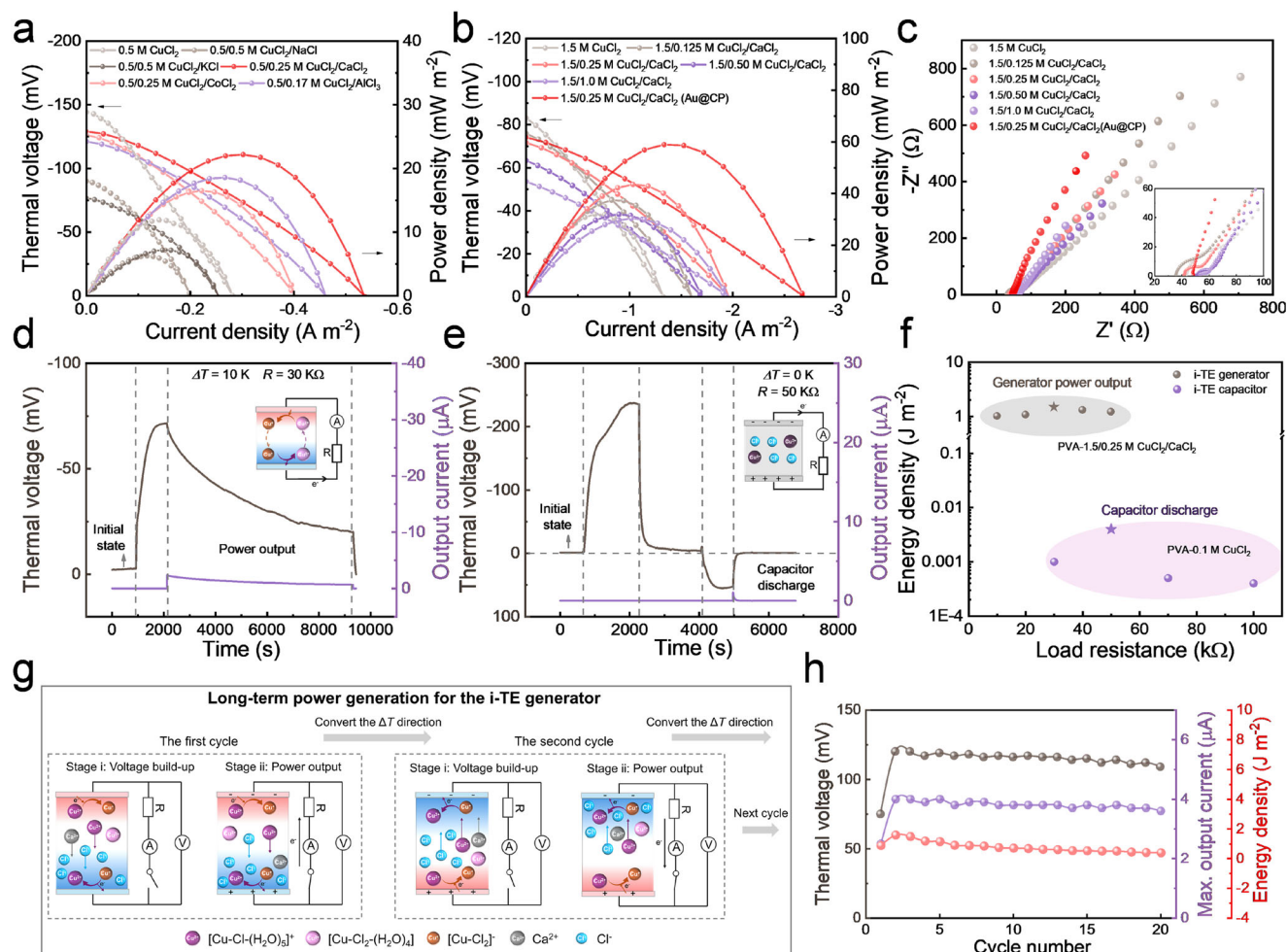


Fig. 5 | Optimization of output performance and long-term power generation.

a Combination curves of thermal voltage, output current density, and instantaneous output power density for PVA-0.5/ x M $\text{CuCl}_2/\text{N-Cl}$ i-TE cells (N: K^+ , Na^+ , Ca^{2+} , Co^{2+} , Al^{3+} , the corresponding x : 0.5, 0.5, 0.25, 0.25, and 0.17 M). **b** Combination curves of thermal voltage, output current density, and instantaneous output power density for PVA-1.5/ x M $\text{CuCl}_2/\text{CaCl}_2$ i-TE cells ($x = 0, 0.125, 0.25, 0.5, \text{ and } 1.0$ M). **c** EIS results of the PVA-1.5/ x M $\text{CuCl}_2/\text{CaCl}_2$ ($x = 0, 0.125, 0.25, 0.5, \text{ and } 1.0$ M) i-TE cells. The inset picture is the enlarged view at high-frequency ranges. **d** Output

voltage and current of the CP | PVA-1.5/0.25 M $\text{CuCl}_2/\text{CaCl}_2$ | CP using an i-TE generator working mode. **e** Output voltage and current of the CP | PVA-0.1 M CuCl_2 | CP using an i-TE capacitor working mode. **f** Energy harvesting comparison of the i-TE generator and capacitor with different load resistances. **g** Diagram of the long-term power generation working mode for the i-TE generator. **h** Comparisons of thermal voltage, maximum output current, and energy density of CP | PVA-1.5/0.25 M $\text{CuCl}_2/\text{CaCl}_2$ | CP i-TE cell for long-term power generation. The total cycle number is twenty.

adjusted in the PVA-1.5/ x M $\text{CuCl}_2/\text{CaCl}_2$ ($x = 0.125, 0.25, 0.5, \text{ and } 1.0$ M) i-TE cells. The MD result shows little regulation in [Cu-Cl] coordination species upon adding 0.25 M CaCl_2 , indicating that the increased Cl^- shows a dominant role in stabilizing Cu^+ during the redox reaction (Supplementary Fig. 36). A 40-nm-thick gold layer was deposited on carbon paper electrodes (Au@CP) to further accelerate the electron transfer process⁴⁶. The highest P_{max} value of 60 mW m^{-2} was achieved in Au@CP | PVA-1.5/0.25 M $\text{CuCl}_2/\text{CaCl}_2$ | Au@CP i-TE cell (Fig. 5b). The opposite trend between V_{oc} and I_{sc} also showed the trade-off relationship as increasing Cl^- content. The EIS plots showed a continuous decrease in R_{ct} with increasing CaCl_2 concentrations and modifying carbon paper electrodes (Fig. 5c), indicating the facilitation of redox reaction near the electrode interface. Except for P_{max} , the continuous energy harvesting and output were illustrated using the i-TE generator and capacitor working modes (Supplementary Fig. 37). The i-TE generator of the CP | PVA-1.5/0.25 M $\text{CuCl}_2/\text{CaCl}_2$ | CP cell showed a continuous voltage and current output at a ΔT of 10 K (Fig. 5d). The highest energy density of 2 h (E_{2h}) of 1.5 J m^{-2} was achieved when loading an external resistance of 30 k Ω (Supplementary Fig. 38). The heat-to-energy efficiency of the i-TE generator was calculated at $\eta = 0.02\%$ (as

detailed in Supplementary Note 6 and Supplementary Fig. 39). The i-TE capacitor of the CP | PVA-0.1 M CuCl_2 | CP cell showed a charge storage property at a ΔT of 10 K and capacitor discharging without ΔT (Fig. 5e). The highest energy density of 1 h (E_{1h}) of 0.004 J m^{-2} was achieved when loading a 50 k Ω resistance (Supplementary Fig. 40). The i-TE generator showed a significant advantage in continuous power output, compared with the energy storage property by using the i-TE capacitor mode (Fig. 5f). We also tested the long-time (4 h) output current and calculated normalized output electric charge factors, showing a significantly enhanced thermogalvanic redox contribution with increased CuCl_2 concentrations (Supplementary Fig. 41). Under near-short-circuit conditions, the CP | PVA-1.0 M CuCl_2 | CP i-TE cell exhibited a high short-circuit current (I_{sc}) peak value of $181 \mu\text{A}$ and continuous I_{sc} (approximately $0.8 \mu\text{A}$) output for 1 hour, showing the sustained redox-cycled self-current in high-concentration composition (Supplementary Fig. 42). Furthermore, twenty cycles were performed to show the sustainable heat-to-energy conversion of the i-TE generator. In the long-term power generation, the reactivation stage is modified from self-recovery to drive at a reverse ΔT and directly connected with the voltage build-up stage of the next cycle without rest (Fig. 5g, as

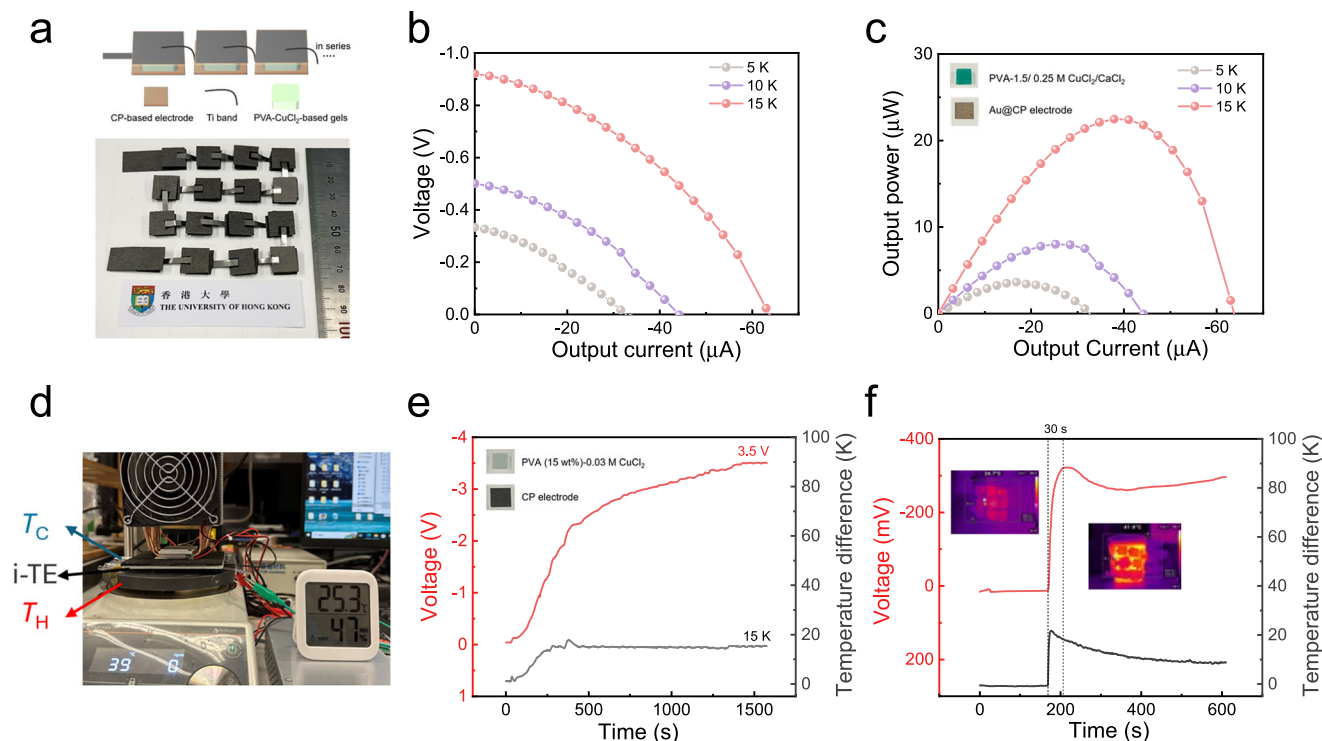


Fig. 6 | i-TE module composed of 16 units in series. **a** Schematic diagram and real picture of the module. **b** Output voltage. **c** Output power versus output current to the i-TE generator module with the ΔT of 5, 10, and 15 K. The i-TE gel and electrode of the module are PVA-1.5/0.25 M $\text{CuCl}_2/\text{CaCl}_2$ gel and Au@CP, respectively. **d** Powering the thermohydrometer with no additional voltage booster when

harvesting a ΔT of 20 K. **e** Voltage generated from the i-TE capacitor module when harvesting a temperature difference of 15 K. The i-TE gel and electrode of the module are PVA (15 wt%)-0.03 M CuCl_2 gel and CP, respectively. **f** Demonstration of thermal voltage generated by a 9-cell capacitor module from a cup with warm water.

detailed in Supplementary Note 7). The curve of long-term output voltage and current versus time is shown in Supplementary Fig. 43. The thermal voltage and maximum output current showed a retention of 91% and 90%, respectively, after a 20-cycle power generation. The total harvesting output energy density of the long-time duration test (nearly 30 h) is 15.9 J m^{-2} , suggesting the potential application in the self-powered wearable sensors (Fig. 5h). The good cycle performance showed the reversibility of the $[\text{Cu-Cl}_y\text{-(H}_2\text{O)}_{6-y}]^{2+}/[\text{Cu-Cl}_2]^-$ redox couple and sustainable long-term service of the i-TE cells.

16-cell i-TE module

Finally, a 16-cell i-TE module was assembled in series, as shown in (Fig. 6a). Here, PVA-1.5/0.25 M $\text{CuCl}_2/\text{CaCl}_2$ gel with Au@CP electrode and PVA (15 wt%)-0.03 M gel with CP electrode were used as i-TE units to fabricate two types of modules, called the generator and capacitor module, respectively. The V_{oc} , I_{sc} , and P_{max} produced by the generator module were 0.9 V, $60 \mu\text{A}$, and $22 \mu\text{W}$, respectively, with a ΔT of 15 K (Fig. 6b, c). The module could directly drive a thermohydrometer when harvesting a ΔT of 20 K (Fig. 6d), owing to its high output power. Figure 6e showed the ultrahigh thermal voltage of 3.5 V generated with a ΔT of 15 K using a capacitor module (Fig. 6e). The generated voltage is enough to drive different sensors without additional DC-DC voltage boosters, such as pressure sensors (1.3 to 3.6 V), humidity sensors (1.6 to 3.6 V), and gas sensors (1.8 to 3.6 V)¹⁴. We also demonstrated a showcase for heat-to-energy conversion by attaching a 9-cell capacitor module to a cup containing warm water, showing a sustainable output voltage of approximately 320 mV (Fig. 6f). Furthermore, the quick thermal charging time of 30 s exhibits a quick response of the i-TE module to temperature fluctuation. The high-performance n-type i-TE gels reveal great potential for applications in low-grade heat harvesting, temperature monitoring, and sensing.

Discussion

In this work, we uncover the overlooked thermogalvanic effect in CuCl_2 i-TE materials and report a new n-type redox couple of $\text{Cu}^{2+}/\text{Cu}^+$ stabilized by Cl^- , which can surpass other widely used thermogalvanic systems. By combining shell-isolated nanoparticle-enhanced Raman spectroscopy (SHINERS) with XPS and XANES valence-state analysis, the first quantitative, spatially resolved tracking of redox speciation is provided under operando conditions. This methodology resolves longstanding ambiguities in correlating coordination environments (e.g., $[\text{Cu-Cl}]$ bond dynamics) with redox reaction states, offering a blueprint for studying ion-coupled electron transfer in complex soft matrices. A thermo-diffusion/galvanic i-TE coupling driven by $[\text{Cu-Cl}]$ speciation is validated in PVA- x CuCl_2 gels (x : CuCl_2 concentrations). Leveraging coordination chemistry to tune ion species, a giant thermopower of -30.6 mV K^{-1} and a remarkable power density of $0.6 \text{ mW m}^{-2} \text{ K}^{-2}$ are achieved. We demonstrate a high thermal voltage of 3.5 V and output power of $22 \mu\text{W}$ in the 16-cell modules when harvesting low-grade heat. Such i-TE materials could revolutionize applications ranging from self-powered wearable sensors to large-area waste heat recovery systems, where flexibility, scalability, and efficiency are paramount. Our findings underscore the untapped potential of coordination chemistry in designing next-generation energy materials.

Methods

Materials

The raw materials are shown as follows: poly (vinyl alcohol) ($MW = 89000 - 98000$, 95%), CuSO_4 ($MW = 159.61$, 99%), $\text{Cu}(\text{NO}_3)_2 \cdot x\text{H}_2\text{O}$ ($MW = 187.56$, 99.0%), Na_2SO_4 ($MW = 142.04$, 99.5%), KCl ($MW = 74.55$, 99.5%), CaCl_2 ($MW = 110.98$, 99.99%), MgCl_2 ($MW = 95.21$, 99.99%), CuCl_2 ($MW = 134.45$, 98%), ZnCl_2 ($MW = 136.3$, 99.95%), $\text{CoCl}_2 \cdot 6\text{H}_2\text{O}$

($MW = 237.93$, 99.99%), NiCl_2 ($MW = 129.6$, 99%) were provided by Macklin Biochemical CO., Ltd. NaCl ($MW = 58.44$, 99.5%), AlCl_3 ($MW = 133.34$, 99%) were purchased from Aladdin Industrial Corporation. Carbon paper (TGP-H-060) was purchased from Toray Industries, Inc. (Japan).

Preparation of PVA hydrogel

The PVA hydrogel was prepared by using the freeze-thaw method. In this work, we regulated the weight ratio of PVA to water ($r_w = 7.5\%$, 10% , 12.5% , and 15%). As an example, for preparing 10 wt% PVA hydrogel, 6 g of PVA powder was first dissolved and stirred in 54 mL DI water for 30 min. Then, the PVA solution was heated and stirred in a water bath at 95°C for 6 h. Finally, the as-prepared solution was defoamed and poured into a mold (size: $15\text{ mm} \times 15\text{ mm} \times 3\text{ mm}$ (length \times width \times height)), frozen at -20°C for 6 h and thawed at 25°C for 1 h, repeating three times, to obtain the PVA hydrogel. The mold was prepared by using the Bambu Lab X1E 3D printer.

Preparation of PVA-based i-TE gels

The general formula of the i-TE gels was PVA (r_w)- x MX (x : the molar concentration of MX salts; MX = NaCl , KCl , CuSO_4 , $\text{Cu}(\text{NO}_3)_2$, CuCl_2 , CaCl_2 , ZnCl_2 , MgCl_2 , CoCl_2 , NiCl_2 , and AlCl_3). All the i-TE gels in this work were prepared via immersing the PVA hydrogels in the corresponding salt solutions. As an example, for preparing the PVA (10 wt%)-1.5/0.25 M $\text{CuCl}_2/\text{CaCl}_2$ i-TE gel: firstly, the 10 wt% PVA hydrogel was prepared as the above method; then 4.034 g CuCl_2 and 0.555 g CaCl_2 were dissolved into 20 mL DI water to obtain the mixture salt solution; finally, the PVA hydrogel was immersed in the solution for 12 h and obtained the i-TE gel.

Fabrication of i-TE cells

Carbon paper was used as the electrodes for assembling the i-TE cells with a 3 mm-thick sandwich structure CP|i-TE gel|CP. The size of the as-prepared i-TE gel is $15\text{ mm} \times 15\text{ mm} \times 3\text{ mm}$, and the size of the carbon paper is $25 \times 25\text{ mm}$. The cell molds are identical to those used in the PVA preparation process. To optimize the output power, gold-coated carbon paper was also employed as electrodes⁴⁶. Gold (Au) sputtering on the carbon paper was conducted using a Denton Vacuum Desktop Pro system at an argon pressure of 20 m Torr and an operating power of 120 W for 40 s, resulting in a film thickness of approximately 40 nm. The as-fabricated i-TE cell was encapsulated in a polyethylene film using a hot press machine to prevent the gel from losing water.

Fabrication of the i-TE module

The 16-cell module was assembled in series using titanium (Ti) taps. The size of each i-TE unit was $10\text{ mm} \times 10\text{ mm} \times 3\text{ mm}$, which can be uniformly prepared by the 3D-printed molds. The size of Au@CP and the CP electrode was $11 \times 11\text{ mm}$. The as-fabricated i-TE module was encapsulated in a polyethylene film using a hot press machine. The temperature difference was generated by the heat plate and the semiconductor cooling platform. Other performance tests are the same as those of the i-TE cell.

Ultraviolet-visible (UV-vis) spectroscopy (Integrating Sphere) characterization

The Ultraviolet-visible (UV-vis) spectroscopy was conducted on an Agilent Cary 5000 spectrometer using an integral ball accessory. The absorption signals of UV-vis are always unlimited when the CuCl_2 concentrations are higher than 0.1 M. Herein, an integrating sphere was employed to select the diffuse reflection signals of i-TE gels and then to achieve the corresponding absorption intensity. The size of the gels is $15\text{ mm} \times 15\text{ mm} \times 0.5\text{ mm}$. In this work, all the UV-vis spectra of the gels were obtained by using this method.

X-ray photoelectron spectroscopy (XPS) characterization

The XPS test was conducted on a Thermo-Scientific Escalab QXi microprobe. The gels were immediately taken out from the i-TE cells after thermal charging with a ΔT of 10 K for 30 min and freeze-dried for 48 h to obtain the dried samples. A ΔT of 10 K was constructed from the bottom to the top across the i-TE gel. The gel top is near the cold side of the electrode (T_C) while the gel bottom is near the hot side of the electrode (T_H).

X-ray absorption near-edge structure (XANES) characterization

The XANES spectra at Cu K-edge were performed at BL11B beamline of Shanghai Synchrotron Radiation Facility. The data were obtained under ambient conditions in fluorescence mode for the Cu K-edge. The gel sample is a freeze-dried PVA-0.1 M CuCl_2 gel that has been thermally charged for 30 min. The CuO and Cu_2O were used as the standard samples to confirm the copper electron states in the i-TE gel.

Operando Raman spectra characterization

The Xplora confocal microprobe Raman system (HORIBA) was used to record the Raman spectra. All measurements were performed using a He-Ne laser with an excitation wavelength of 637.8 nm and a 50x long working distance (8 mm) microscope objective with a numerical aperture of 0.55. The Raman frequency was calibrated using a silicon wafer in each experiment. In this study, PVA- CuCl_2 gels containing different concentrations of CuCl_2 (0.01, 0.05, 0.1, 0.5, and 1 M) were placed in a specially designed temperature-controlled Raman cell for operando testing of the gel surface and cross-sections. The temperature difference was controlled at 10 K, crossing from the bottom to the top in the gel top surface test, and from left to right in the cross-section test, respectively. The humidity was maintained at 60%. In addition, PVA-0.01 M CuCl_2 gel was soaked in heavy water (D_2O) for 12 h, and isotopes were used to confirm that the peak at 420 cm^{-1} is the Cu-O stretching vibration of $[\text{Cu-H}_2\text{O}]$. Here, we defined a normalized $[\text{Cu-Cl}]$ factor to quantify the coordination species change. For the original state of PVA-0.1 M CuCl_2 i-TE gels, the Raman peak from 215.2 to 296.5 cm^{-1} of $[\text{Cu-Cl}]$ species, and the corresponding integration area was 11717. We defined the $[\text{Cu-Cl}]$ factor of this state as 1. The factors at different reaction times could be calculated by making a ratio between the integrated $[\text{Cu-Cl}]$ peak area with 11717. Taking PVA-0.1 M CuCl_2 gel as an example, as the thermal charging time increased from 5 to 10, 15, 20, 25, and 30 mins, the integrated $[\text{Cu-Cl}]$ Raman peak area was 13357, 16404, 23786, 31402, 36557, and 41947, respectively, corresponding to the normalized $[\text{Cu-Cl}]$ factor increased from 1 to 1.14, 1.40, 2.03, 2.68, 3.12, and 3.58. The normalized $[\text{Cu-Cl}]$ factors of other samples with different CuCl_2 concentrations were achieved by using the same method.

Electrochemical characterization

The electrochemical characterization, including Cyclic voltammetry (CV) and Electrochemical Impedance Spectroscopy (EIS) test, was measured on an electrochemical workstation (Admiral Instruments, America). For aqueous salt solutions, CV test scanning from -0.6 V to $+0.8\text{ V}$ was conducted with a three-electrode configuration, carbon paper (size: $1.5\text{ cm} \times 1.5\text{ cm}$) was used as the working electrode and platinum (size: $1\text{ cm} \times 1\text{ cm}$) and Ag/AgCl electrodes were used as the counter and reference electrodes, respectively. 2 M Na_2SO_4 was employed as the supporting electrolyte in aqueous media to reduce the ohmic overpotential. For symmetrical i-TE cells, CV test scanning from -0.6 and $+0.6\text{ V}$ was conducted with a two-electrode configuration, in which one carbon paper electrode served as the working electrode while another was employed as the counter and reference electrodes simultaneously. The EIS was adopted to analyze the resistance properties of the cells between 0.05 Hz to 10000 Hz at the AC amplitude of 10 mV. The ionic conductivities of gels were calculated

using Eq. 1

$$\sigma = l/RS \quad (1)$$

where l , S , and R are the thickness, the cross-sectional area, and the resistance of the i-TE cells, respectively. The R was the first interception of the high-frequency semicircle (fitted R_s) in the results of the EIS measurement.

I-TE performance measurement. The ionic thermoelectric performance was measured using an Ionic Thermoelectric Testing System (ITTS, PURI Materials). The thermal voltage (ΔV) and temperature difference (ΔT) were recorded using a built-in test program. Thermopower was the slope of ΔV versus ΔT . The thermopower (S_i) was calculated according to Eq. 2:

$$S_i = -\frac{V(T_H) - V(T_C)}{T_H - T_C} \quad (2)$$

Where S_i is the thermopower, $V(T_H)$ and $V(T_C)$ are the potential at the hot side and cold sides of the i-TE cells, respectively. T_H and T_C are the temperatures at the hot and cold sides of the i-TE cells, respectively. The ΔT was set to 1, 2, 3, 4, and 5 K, and the cold side (T_C) was maintained at 298.15 K.

The instantaneous output power was measured using a Keithley-2400 at a voltage-current (V - I) discharge at a ΔT of 10 K. T_C was fixed at 298.15 K. For normalized maximum power density, the distance between the two electrodes was 0.3 cm, and the cross-sectional area of the electrode was 2.25 cm^2 . The normalized instantaneous output power density (P_{max}) was calculated according to Eq. 3:

$$P_{\text{max}} = \frac{V_{\text{oc}} I_{\text{sc}}}{4} \quad (3)$$

Where V_{oc} and I_{sc} are the open-circuit voltage and short-circuit density, respectively.

The continuous output voltage and current were measured using the ITTS at a ΔT of 10 K. T_C was fixed at 298.15 K. The energy density (E) was calculated according to Eq. 4:

$$E = \int_0^t V(t)I(t)dt \quad (4)$$

Where the $V(t)$ and $I(t)$ are the output voltage and current dependent on t , t is the output power time.

Data availability

The source data generated in this study are provided in the Source Data file, and any additional data will be available upon request from the corresponding author. Source data are provided in this paper.

References

- Yu, B. et al. Thermosensitive crystallization-boosted liquid thermocells for low-grade heat harvesting. *Science* **370**, 342–346 (2020).
- Wang, Y. et al. In situ photocatalytically enhanced thermogalvanic cells for electricity and hydrogen production. *Science* **381**, 291–296 (2023).
- Duan, J. et al. Liquid-state thermocells: Opportunities and challenges for low-grade heat harvesting. *Joule* **5**, 768–779 (2021).
- He, W. et al. High thermoelectric performance in low-cost $\text{SnS}_{0.91}\text{Se}_{0.09}$ crystals. *Science* **365**, 1418–1424 (2019).
- Dobashi, Y. et al. Piezoionic mechanoreceptors: Force-induced current generation in hydrogels. *Science* **376**, 502–507 (2022).
- Liu, S. et al. Quadruple-band synglisis enables high thermoelectric efficiency in earth-abundant tin sulfide crystals. *Science* **387**, 202–208 (2025).
- Sun, S., Li, M., Shi, X. & Chen, Z. Advances in ionic thermoelectrics: from materials to devices. *Adv. Energy Mater.* **13**, 2203692 (2023).
- Yu, M. et al. Ionic thermoelectric gels and devices: Progress, opportunities, and challenges. *EnergyChem.* **6**, 100123 (2024).
- Li, Q. et al. Anionic entanglement-induced giant thermopower in ionic thermoelectric material Gelatin- $\text{CF}_3\text{SO}_3\text{K}$ - $\text{CH}_3\text{SO}_3\text{K}$. *eScience* **3**, 100169 (2023).
- He, Y. et al. Role of ions in hydrogels with an ionic Seebeck coefficient of 52.9 mV K^{-1} . *J. Phys. Chem. Lett.* **13**, 4621–4627 (2022).
- Li, T. et al. Cellulose ionic conductors with high differential thermal voltage for low-grade heat harvesting. *Nat. Mater.* **18**, 608–613 (2019).
- Yang, P. et al. Wearable thermocells based on gel electrolytes for the utilization of body heat. *Angew. Chem.* **128**, 12229–12232 (2016).
- Zhang, D. et al. Boosting Thermoelectric performance of thermogalvanic hydrogels by structure engineering induced by liquid nitrogen quenching. *Adv. Energy Mater.* **14**, 2303358 (2023).
- Han, C.-G. et al. Giant thermopower of ionic gelatin near room temperature. *Science* **368**, 1091–1098 (2020).
- Zhao, W. et al. Exceptional n-type thermoelectric ionogels enabled by metal coordination and ion-selective association. *Sci. Adv.* **9**, eadk2098 (2023).
- Chen, B. et al. Specific behavior of transition metal chloride complexes for achieving giant ionic thermoelectric properties. *NPJ Flex Electron* **6**, 79 (2022).
- Wu, Z. et al. Advanced bacterial cellulose ionic conductors with gigantic thermopower for low-grade heat harvesting. *Nano Lett.* **22**, 8152–8160 (2022).
- Liu, Y. et al. Advanced wearable thermocells for body heat harvesting. *Adv. Energy Mater.* **10**, 2002539 (2020).
- Taheri, A., MacFarlane, D. R., Pozo-Gonzalo, C. & Pringle, J. M. Application of a water-soluble cobalt redox reaction couple in free-standing cellulose films for thermal energy harvesting. *Electrochim. Acta* **297**, 669–675 (2019).
- Han, Y., Zhang, J., Hu, R. & Xu, D. High-thermopower polarized electrolytes enabled by methylcellulose for low-grade heat harvesting. *Sci. Adv.* **8**, eabl5318 (2022).
- Zhou, H., Yamada, T. & Kimizuka, N. Supramolecular thermo-electrochemical cells: enhanced thermoelectric performance by host-guest complexation and salt-induced crystallization. *J. Am. Chem. Soc.* **138**, 10502–10507 (2016).
- Stricker, E. A., Krueger, K. W., Savinell, R. F. & Wainright, J. S. Investigating a bromide supported electrolyte for an all-copper flow battery. *J. Electrochem. Soc.* **165**, A1797–A1804 (2018).
- Sanz, L., Palma, J., García-Quismondo, E. & Anderson, M. The effect of chloride ion complexation on reversibility and redox reaction potential of the Cu(II)/Cu(I) couple for use in redox reaction flow batteries. *J. Power Sourc.* **224**, 278–284 (2013).
- Hu, J. et al. Double selective ionic gel with excellent thermopower and ultra-high energy density for low-quality thermal energy harvesting. *Energy Environ. Sci.* **17**, 1664–1676 (2024).
- Liu, S. et al. Giant and bidirectionally tunable thermopower in nonaqueous ionogels enabled by selective ion doping. *Sci. Adv.* **8**, eabj3019 (2022).
- Yu, B. et al. Cost-effective n-type thermocells enabled by thermosensitive crystallizations and 3D multi-structured electrodes. *Nano Energy* **93**, 106795 (2022).
- Kim, B., Hwang, J. U. & Kim, E. Chloride transport in conductive polymer films for an n-type thermoelectric platform. *Energy Environ. Sci.* **13**, 859–867 (2020).

28. Chen, B., Zhang, X., Yang, J., Feng, J. & Wang, T. Giant Negative Thermopower enabled by bidirectionally anchored cations in multifunctional polymers. *ACS Appl. Mater. Interfaces* **15**, 24483–24493 (2023).
29. Sun, X. et al. Boosting negative thermopower of chitosan hydrogel via bio-inspired anisotropic porous. *Adv. Funct. Mater.* **35**, 2419762 (2025).
30. Yu W. et al. Exceptional n-type ionic thermoelectric hydrogels by synergistic hydrophobic and coordination interactions. *Adv. Mater.* **37**, e10199 (2025).
31. Zhang, X. et al. Manipulating coordination environment for a high-voltage aqueous copper-chlorine battery. *Nat. Commun.* **14**, 6738 (2023).
32. Yang, C. et al. Copper-coordinated cellulose ion conductors for solid-state batteries. *Nature* **598**, 590–596 (2021).
33. Li, Y. et al. Realizing record-high output power in flexible gelatin/GTA-KCl-FeCN^{4+/3-} ionic thermoelectric cells enabled by extending the working temperature range. *Energy Environ. Sci.* **15**, 5379–5390 (2022).
34. Li, Y. et al. 3D hierarchical electrodes boosting ultrahigh power output for gelatin-KCl-FeCN^{4+/3-} ionic thermoelectric cells. *Adv. Energy Mater.* **12**, 2103666 (2022).
35. Li, Y.-Y., Wang, M., Wang, C.-C., Zhang, Q.-W. & Yi, H.-B. Distinctive hydration dynamics around highly coordinated Cu²⁺/Zn²⁺-chloride complexes: A molecular dynamics simulation study. *J. Mol. Liquids* **314**, 113619 (2020).
36. Chi, C. et al. Reversible bipolar thermopower of ionic thermoelectric polymer composite for cyclic energy generation. *Nat Commun* **14**, 306 (2023).
37. Li, J. F. et al. Shell-isolated nanoparticle-enhanced Raman spectroscopy. *Nature* **464**, 392–395 (2010).
38. Wang, Y.-H. et al. In situ Raman spectroscopy reveals the structure and dissociation of interfacial water. *Nature* **600**, 81–85 (2021).
39. Archibald, S. M., Migdisov, A. A. & Williams-Jones, A. E. An experimental study of the stability of copper chloride complexes in water vapor at elevated temperatures and pressures. *Geochim. et Cosmochim. Acta* **66**, 1611–1619 (2002).
40. Powell, K. J. et al. Chemical speciation of environmentally significant metals with inorganic ligands Part 2: The Cu²⁺-OH⁻, Cl⁻, CO₃²⁻, SO₄²⁻, and PO₄³⁻ systems (IUPAC Technical Report). *Pure Appl. Chem.* **79**, 895–950 (2007).
41. Zhang, N., Zeng, D., Hefter, G. & Chen, Q. Chemical speciation in concentrated aqueous solutions of CuCl₂ using thin-film UV-visible spectroscopy combined with DFT calculations. *J. Mol. Liquids* **198**, 200–203 (2014).
42. Mereshchenko, A. S. et al. Photochemistry of copper (II) chlorocomplexes in acetonitrile: Trapping the ligand-to-metal charge transfer excited state relaxation pathways. *Chem. Phys. Lett.* **615**, 105–110 (2014).
43. Yi, H.-B., Xia, F.-F., Zhou, Q. & Zeng, D. [CuCl₃]⁻ and [CuCl₄]²⁻ Hydrates in Concentrated Aqueous Solution: A density functional theory and ab initio study. *J. Phys. Chem. A* **115**, 4416–4426 (2011).
44. Greenacre, M. et al. Principal component analysis. *Nat. Rev. Methods Primers* **2**, 100 (2022).
45. Brugger, J. & BeerOz, A set of Matlab routines for the quantitative interpretation of spectrophotometric measurements of metal speciation in solution. *Comput. Geosci.* **33**, 248–261 (2007).
46. Wang, S. et al. High-performance cryo-temperature ionic thermoelectric liquid cell developed through a eutectic solvent strategy. *Nat. Commun.* **15**, 1172 (2024).
- Photonic Manufacturing, funded by The Hong Kong Jockey Club Charities Trust. Y.L. and N.F. also appreciate startup funding from the Materials Innovation Institute for Life Sciences and Energy (MILES), HKU-SIRI in Shenzhen, which supports this manuscript. W.L. acknowledges support from the NSFC program for Distinguished Young Scholars (T2425012), the Shenzhen Innovation Program for Distinguished Young Scholars (RCJC20210706091949018), and the Guangdong Provincial Key Laboratory Program (2021B1212040001). J.-F.L. and Y.-H.W. acknowledge support from the National Natural Science Foundation of China (22472141, 22322206, 22525042, and T2293692) and the Industry-University-Research Joint Innovation Project of Fujian Province, China (2025H6023). J.L. acknowledges support from the Australian Research Council Discovery Project (DP210103888).

Author contributions

N.F. conceived and supervised the project. Y.L. designed and conducted the experiment, analyzed the results, and wrote the manuscript. Y.-R.Q., Y.-H.W., and J.-F.L. carried out the operando SHINERS test. J.L. and Z.L. (Jefferson) performed the molecular dynamics simulations. H.L. provided the density functional theory calculation. Z.L. conducted the principal component analysis. Y.C. and L.X. experimented with sputtering Au nanoparticles on carbon electrodes. M.Y. experimented with testing the thermal conductivity of i-TE gels. C.L. and W.L. provided comments for the manuscript. All authors analyzed the results and contributed to the optimization of the manuscript.

Competing interests

The authors declare no competing interests.

Additional information

Supplementary information The online version contains supplementary material available at <https://doi.org/10.1038/s41467-026-68721-9>.

Correspondence and requests for materials should be addressed to Yao-Hui Wang or Nicholas X. Fang.

Peer review information *Nature Communications* thanks Wei Zeng, and the other anonymous reviewer(s) for their contribution to the peer review of this work. A peer review file is available.

Reprints and permissions information is available at <http://www.nature.com/reprints>

Publisher's note Springer Nature remains neutral with regard to jurisdictional claims in published maps and institutional affiliations.

Open Access This article is licensed under a Creative Commons Attribution-NonCommercial-NoDerivatives 4.0 International License, which permits any non-commercial use, sharing, distribution and reproduction in any medium or format, as long as you give appropriate credit to the original author(s) and the source, provide a link to the Creative Commons licence, and indicate if you modified the licensed material. You do not have permission under this licence to share adapted material derived from this article or parts of it. The images or other third party material in this article are included in the article's Creative Commons licence, unless indicated otherwise in a credit line to the material. If material is not included in the article's Creative Commons licence and your intended use is not permitted by statutory regulation or exceeds the permitted use, you will need to obtain permission directly from the copyright holder. To view a copy of this licence, visit <http://creativecommons.org/licenses/by-nc-nd/4.0/>.

© The Author(s) 2026

Acknowledgements

Y.L. and N.F. acknowledge the seed project for PI research supported by the Hong Kong University Research Council. The Fang group's research at HKU is conducted in the JC STEM Lab of Scalable and Sustainable